energies

MDPI

Article

Dynamic Modeling and Comparison Study of Control Strategies of a Small-Scale Organic Rankine Cycle

Yuhao Zhou [1,2,3], Jiongming Ruan [3], Guotong Hong [1,2,*] and Zheng Miao [4,*]

[1] Key Laboratory of Technology on Space Energy Conversion, Technical Institute of Physics and Chemistry, Chinese Academy of Sciences, Beijing 100190, China; yuhao-zhou@chder.com
[2] University of Chinese Academy of Sciences, Beijing 100049, China
[3] Huadian Electric Power Research Institute Co., Ltd., Hangzhou 310030, China; jiongming-ruan@chder.com
[4] Beijing Key Laboratory of Multiphase Flow and Heat Transfer for Low-Grade Energy Utilization, North China Electric Power University, Beijing 102206, China
* Correspondence: gthong@mail.ipc.ac.cn (G.H.); miaozheng@ncepu.edu.cn (Z.M.)

Abstract: The control strategy is crucial for the effective and safe operation of the ORC system. A transient model of the ORC system was developed in the present work and validated by the experimental data of a 4 kW ORC prototype. Then, the effect of heat source temperature on the dynamic response and operation characteristics of the ORC system were analyzed. Five control strategies were compared: the constant working fluid mass flow rate mode, constant vapor superheat mode, constant vapor temperature mode, constant evaporation pressure mode and constant output power load mode. Under the constraint that the working fluid at the expander inlet should be superheated, we found that the constant vapor superheat mode enabled the safe operation with the largest range of heat source temperature, while the other four modes were only available for a certain temperature range. Apart from the constant output power mode, the constant evaporation pressure mode can also provide a relatively stable performance for the ORC unit. The variation of the thermal efficiency was limited when the heat source temperature was higher than 125 °C, except for the constant vapor temperature mode. Considering the high performance and stable operation of the ORC system, it is necessary to have different operation modes combined in the control strategy according to the specific working scenarios.

Keywords: organic Rankine cycle; dynamic modeling; control strategy; output power; thermal efficiency

Citation: Zhou, Y.; Ruan, J.; Hong, G.; Miao, Z. Dynamic Modeling and Comparison Study of Control Strategies of a Small-Scale Organic Rankine Cycle. *Energies* **2022**, *15*, 5505. https://doi.org/10.3390/en15155505

Academic Editor: Alon Kuperman

Received: 4 July 2022
Accepted: 27 July 2022
Published: 29 July 2022

1. Introduction

The organic Rankine cycle (ORC) is a promising technology to convert low-grade waste heat or renewable heat into mechanical work due to its relatively high efficiency, simple configuration and appropriate working pressure. The steam Rankine cycle uses water as the working fluid, whereas the ORC can generate electricity by using the substance with a low boiling temperature to utilize low-temperature thermal energy at 60~300 °C [1], such as solar energy [2], geothermal energy [3], biomass energy [4] and ocean temperature difference energy [5]. Furthermore, ORC can recover industrial waste heat [6] and engine waste heat [7], thereby, enhancing the overall energy usage efficiency.

In recent years, scholars have conducted extensive research on the ORC, the majority of which focuses on system analysis [8], working fluid screening [9], parameter optimization [10], cycle structure improvement [11], the combine power systems [12] and component structure design [13,14] under system design conditions, while others focus on the off-design characteristics [15]. Heat sources, such as solar energy, geothermal energy and industrial waste heat, are not steady in practice, and their temperature and mass flow rate might fluctuate due to external factors.

Furthermore, the ambient temperature varies with time. As a result, the ORC system always operates in off-design conditions. A thorough understanding of the ORC system's off-design features is required for actual system operation and regulation.

Many researchers studied the off-design operating features of the ORC system. Fu et al. [16] studied the performance of ORC systems at off-design heat source temperatures and showed that the output work and thermal efficiency of ORC systems increased approximately linearly with increasing temperature. Feng et al. [17] investigated the operating characteristics of the ORC system when the heat source temperature varied between 383.15 and 413.15 K. They claimed that the overall performance of the pump, expander, evaporator and condenser all increased with increasing heat source temperature, while the isentropic efficiency of the expander decreased slightly.

Du et al. [18] compared the off-design performance of two ORC systems, single-pressure evaporation and dual-pressure evaporation. The results showed that the net output power decreased by 23% with the heat source flow rate reduced by 30% from the design point and the reduction of the net output power was 39% when the heat source temperature was reduced from 118 to 102 °C.

Manente et al. [19] investigated the off-design performance of an ORC system in subcritical and supercritical cycles with an air-cooled condenser and discovered that the net output work of the system is reduced from 7.7 to 2.7 MW when the geothermal temperature is reduced from 180 to 130 °C. In conclusion, the ORC system's operating characteristics in off-design conditions differ significantly from those under design conditions [20]. Thus, the regulation of operating parameters to ensure the effective and safe operation of the ORC system under off-design situations is important and necessary.

Many scholars participated in the dynamic modeling of the ORC to realize the regulation of the system during off-design situations and control strategies were compared. Colonna et al. [21] built a mathematical model of a biomass power plant boiler and analyzed the system's dynamic performance. The step-wise change of the flue gas flow rate was simulated. Wei et al. [22] compared two modeling approaches based on moving boundary and discretization techniques to build the dynamic model in terms of accuracy, complexity and simulation speed. They claimed that the moving boundary model is more suitable for control design applications due to its faster calculation speed.

Quoilin et al. [23] compared three ORC control strategies: maintaining a constant evaporation temperature, altering the optimal evaporation temperature and regulating the pump speed based on expander speed. The control strategy of the optimal evaporation temperature regulation achieved the best performance, whereas adjusting the mass pump speed according to the expander speed was unable to maintain the ORC system's stable operation under the fluctuating heat source. Wang et al. [24] studied the effect of engine parameters on the dynamic response of the ORC system. Their results revealed that engine conditions had a significant impact on the dynamic response of evaporation pressure, mass enthalpy and superheat at the evaporator outlet, while the condensation pressure remained relatively constant.

Usman et al. [25] employed a PI controller with feedforward and overrun hysteresis compensation to manage the operation of the expander with a sliding pressure control approach, which improves control for systems with high thermal inertia. Jolevski et al. [26] suggested a control approach that combines PI control with a transfer function to convert control errors into control inputs. The results indicated that when the system was perturbed by a 10% reduction in hot oil flow, the proposed control structure had good anti-disturbance capacity.

Wu et al. [27] compared the control performance of an ORC system with and without a feedforward compensation PI controller, finding that the PI controller with feedforward compensation had a stronger anti-disturbance ability. Badescu et al. [28] studied the transient characteristics of an ORC system recovering waste heat from an internal combustion engine. They found that the mass flow rate of working fluid should be adjusted accord-

ing to the heat input to operate the ORC system continuously under fluctuating heat source conditions.

At the same time, the ORC system's thermal efficiency is essentially constant before and after regulation. Chen et al. [29] analyzed the dynamic response of an ORC system with a zeotropic mixture. The results showed that the dynamic change of the condenser is much smaller than that of the evaporator when the heat source temperature or flow rate changes in a stepwise manner; thus, the condenser can be ignored in the dynamic process.

In addition, some experimental research on ORC prototypes under various conditions has been reported. Pei et al. [30] tested an ORC system with a radial expander of 60,000 rev/min rotating speed and produced an output power of roughly 1 kW. Li et al. [31] developed an ORC system based on a single-stage axial expander that produced 6.07 kW and 58% of the expander's isentropic efficiency at a heat source of 130 °C. There are currently fewer experimental studies on the effects of changes in heat source properties on the operating characteristics of ORC systems [32]. Zhang et al. [33] compared the performance of 3 and 10 kW ORC prototypes and found that the heat source and heat sink primarily affected the pump and expander behaviors and then contributed to the overall performance.

According to the above literature review, it is seen that the dynamic characteristics of the ORC system can change significantly during off-design operation when the heat source conditions vary over a wide range, which may threaten the safe operation of the unit. Therefore, a suitable real-time control strategy is necessary to improve the system performance and ensure the safe operation of the unit. By comparing multiple control strategies, the suitable control strategy satisfying the unit operation requirements could be selected.

Most dynamic models or control strategies in the literature were not validated by experimental data. There is a lack of research on the off-design dynamic characteristics and regulation capabilities of various control strategies for small-scale ORC systems under heat source temperature variation based on the experimental verified dynamic model.

In the present work, a 4 kW ORC prototype adopting refrigerant R245fa as the working fluid was tested at the heat source temperature varying between 120~150 °C to validate the developed dynamic model. Five control strategies based on the dynamic model and the prototype: constant working fluid mass flow rate, constant vapor superheat at expander inlet, constant vapor temperature, constant evaporation pressure and constant power load are compared and analyzed.

2. Description of the Organic Rankine Cycle Prototype

Figure 1 shows the schematic diagram and *T-s* diagram of the developed 4 kW ORC prototype. Figure 2 is the arrangement of the test rig. The conductive thermal oil is used to simulate low-grade heat sources (9-10). The oil is heated in an electrical oil boiler with the capacity of 100 kW and circulated by an oil pump. A closed spray cooling tower installed outside is utilized to release heat to the environment (12-11). Water is sprayed on the top of the tower to the tube bundles, while air is drawn from the bottom and flows upward.

The evaporation of the water outside the tubes can reduce the air temperature, which will enhance the overall heat transfer. The cooling water of the ORC system flows through the tubes and is cooled down. The refrigerant R245fa is adopted as the working fluid, which is pressurized by the diaphragm pump (5-6), delivered to the evaporator and vaporized into high-temperature and high-pressure vapor (6-1). Then, it expands in the expander to generate mechanical work (1-2).

The exhaust vapor is condensed into subcooled liquid in the condenser (2-5) and returns to the storage tank to start the next cycle. The evaporator and condenser both adopt the brazed plate heat exchangers. The expander is a scroll expander with a rated mechanical power of 4 kW.

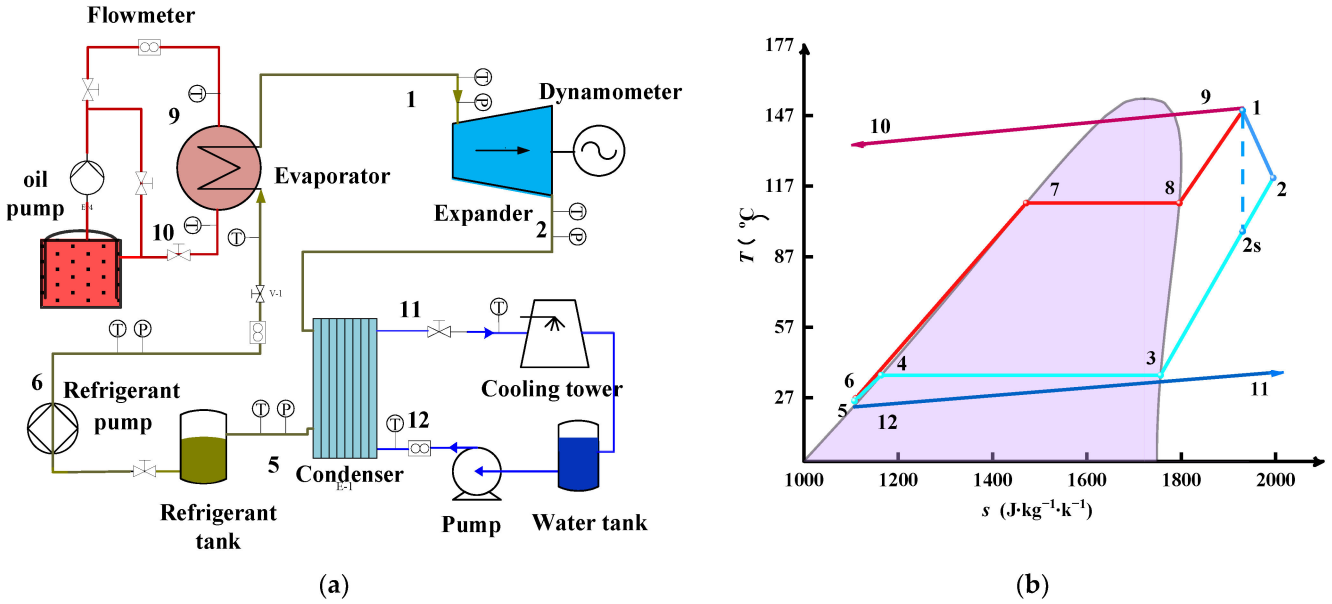

Figure 1. The (**a**) schematic diagram and (**b**) *T*-*s* diagram of the 4 kW ORC prototype.

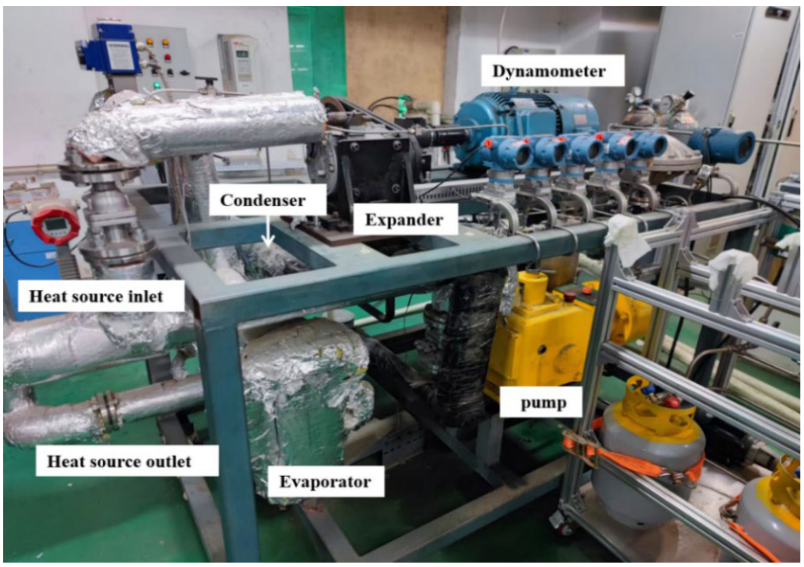

Figure 2. The 4 kW ORC prototype.

The expander is connected to an AC dynamometer by belts and wheels. The AC dynamometer consists of the frequency converter, the asynchronous motor and the sensor of rotating speed and torque. The asynchronous motor is used as the power load of the expander, and its rotating speed can be directly controlled by the frequency converter. Detailed information can be found in our former work [34]. The main features of the ORC components are shown in Table 1. The accuracy of the main sensors is listed in Table 2.

Table 1. The main features of the ORC components.

Component	Type	Featured Parameters	Value
Evaporator	plate heat exchanger	area	5.7 m^2
Condenser	plate heat exchanger	area	4.6 m^2
Expander	Scroll expander	build-in volume ratio	2.3
pump	diaphragm pump	rated mass flow rate	2500 kg/h

Table 2. Accuracy of sensors in the ORC test rig.

Parameters	Sensors	Resolution	Accuracy
Temperature	K-Type Thermocouple	±0.1 °C	±0.5 °C
Pressure	Rosemount Transmitters	±0.1% F.S	±0.1% F.S
Flow Rate	Koch force flow meter	±0.2% F.S	±0.2% F.S
Torque	JN338 torque-tachometer	0.5% F.S	0.5% F.S
Rotational Speed	JN338 torque-tachometer	1 rev/min	1 rev/min

3. Dynamic Models of the Organic Rankine Cycle Prototype

The components of the ORC system were modeled in Simulink and connected according to the processes described in Figure 1. The following are the models of the four main components: evaporator, condenser, pump and expander.

3.1. Evaporator and Condenser Model

The heat transfer processes in the evaporator and condenser are modeled based on the moving boundary model as shown in Figure 3. The moving boundary model is a classical method for the modeling of dynamic characteristics of heat exchangers. It has the advantages of fast calculation and high accuracy [35], which are particularly suitable for the dynamic modeling of a system consists heat exchangers. The following assumptions are established in the moving boundary model:

1. In the heat exchanger, the flow of fluids can be treated as a one-dimensional flow.
2. The pressure distribution is assumed to be uniform along the channel length, ignoring the influence of pressure decrease on the evaporation temperature.
3. We ignore the fluid's and the metal wall's axial heat conduction, assuming that only radial heat transfer exists between the fluid and channel wall.
4. We ignore gravity's effect on the heat transfer.

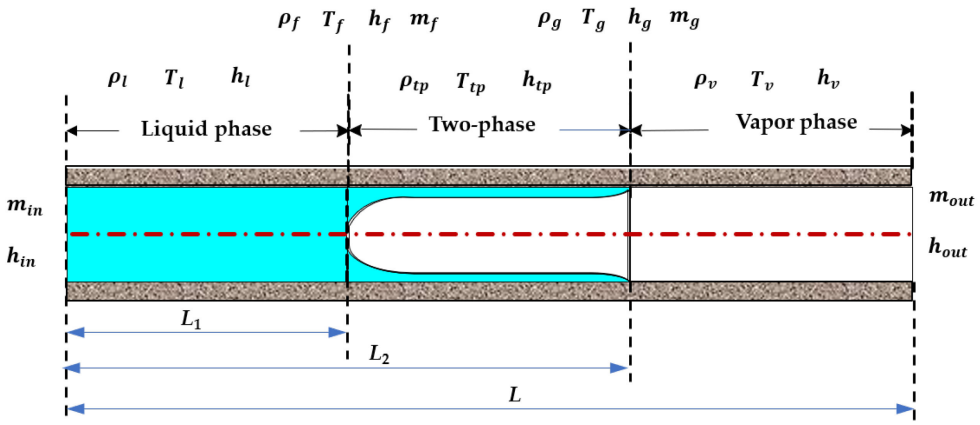

Figure 3. Moving boundary model of the evaporator.

According to the state of the working fluid, the heat transfer process in the evaporator is divided into three sections with changing boundaries: a liquid phase section, a two-phase section and a vapor phase section. Within each section, the lumped parameter method is used, and the dynamic process of the evaporator is obtained by tracking the length change of each phase section.

L_1 is the length of the liquid phase section; L_2 is the length of the heat exchanger from inlet to saturated gas; and L is the total length of the heat exchanger. The subscripts L, s and V stand for the liquid section, two-phase section and vapor phase section, respectively. The subscripts f and g stand for the saturated liquid phase and saturated gas phase, respectively; and the subscripts 'in' and 'out' represent the working fluid inflow and outflow. The conservation equations can be established for each region:

Mass conservation equation:

$$\frac{\partial \rho}{\partial t} + \frac{\partial (\rho v)}{\partial z} = 0 \tag{1}$$

Energy conservation equation:

$$\frac{\partial (\rho h - p)}{\partial t} + \frac{\partial (\rho v h)}{\partial z} = \frac{4}{D_{\mathrm{i}}} \alpha_{\mathrm{i}} (T_{\mathrm{w}} - T) \tag{2}$$

where v is the velocity of the fluid in the channel, and α_{i} is the convective heat transfer coefficient between the fluid and the inside wall.

Using the Leibniz formula [36] to simplify Equations (1) and (2), the expression is:

$$\int_{z_1}^{z_2} \frac{\partial f(z,t)}{\partial t} dz = \frac{d}{dt} \int_{z_1}^{z_2} f(z,t) dz - f(z_2,t) \frac{dz_2}{dt} + f(z_1,t) \frac{dz_1}{dt} \tag{3}$$

By bringing the Leibniz equation into the conservation equation for each phase region and making appropriate simplifications, the moving boundary model for each phase region can be obtained. A detailed derivation process can be found elsewhere [36].

The energy conservation equation of the channel wall in each phase section is given as:

$$c_{\mathrm{w}} \rho_{\mathrm{w}} d_{\mathrm{w}} \frac{dT_{\mathrm{w}}}{dt} = \alpha_{\mathrm{i}} (T_{\mathrm{i}} - T_{\mathrm{w}}) + \alpha_{\mathrm{o}} (T_{\mathrm{a}} - T_{\mathrm{w}}) \tag{4}$$

where α_{o} is the heat transfer coefficient between the hot fluid and the outside wall, c_{w} is the specific heat capacity of the channel wall, and d_{w} is the thickness of the channel wall.

The modeling of the heat transfer process in the condenser also uses the moving boundary method, and the equations and processes are similar to those mentioned above. The derivation process can also be referred to literature [36].

The heat transfer correlations for the evaporator and condenser in each phase region are shown in Table 3, where λ is the thermal conductivity, d_e is the hydraulic diameter, a is the chevron angle, b is the corrugation pitch, Re is the Reynolds number of the fluid, Pr is the Prandtl number of the fluid, and Bo is the boiling number. Detailed expressions of the variables can be found in the literature [37–39].

Table 3. The heat transfer correlations used in the model.

	Evaporator	**Reference**	**Condenser**	**Reference**
Liquid phase	$Nu = 0.2092\mathrm{Re}^{0.78}(\mathrm{Pr})^{1/3}$	[38]	$Nu = 0.317\mathrm{Re}^{0.703}(\mathrm{Pr})^{1/3}$	[37]
Two-phase	$c_1 = 2.81(\frac{b}{d_e})^{-0.041}(\frac{\pi}{2} - \mathrm{a})^{-2.83}$ $c_2 = 0.746(\frac{b}{d_e})^{-0.082}(\frac{\pi}{2} - \mathrm{a})^{-0.61}$ $Nu = c_1 \mathrm{Re}^{c_2} \mathrm{Bo}^{0.3} \mathrm{Pr}^{0.4}$	[40]	$Nu = 4.118\mathrm{Re}^{0.4}\mathrm{Pr}^{1/3}$	[39]
Vapor phase	$Nu = 0.2092\mathrm{Re}^{0.78}(\mathrm{Pr})^{1/3}$	[38]	$Nu = 0.317\mathrm{Re}^{0.703}(\mathrm{Pr})^{1/3}$	[37]
Heat source side	$Nu = 0.724(6\frac{\mathrm{a}}{\pi})^{0.646}\mathrm{Re}^{0.583}(\mathrm{Pr})^{1/3}$			[41]
Cold source side	$Nu = 0.2121\mathrm{Re}^{0.78}(\mathrm{Pr})^{1/3}$			[42]

3.2. Pump Model

The power consumed by the pump can be calculated by:

$$W_{\mathrm{p}} = \frac{W_{\mathrm{p.s}}}{\eta_{\mathrm{p}}} = m_{\mathrm{p}} \frac{(h_{6\mathrm{s}} - h_5)}{\eta_{\mathrm{p}}} = m_{\mathrm{p}} (h_6 - h_5) \tag{5}$$

where $W_{b.s}$ is the power consumption corresponding to the isentropic compression, m_p is mass flow rate. η_p is the isentropic efficiency of the pump and is given as:

$$\eta_p = \eta_{p,d}\left(\frac{m_p}{m_d}\right)^n \tag{6}$$

where $\eta_{p,d}$ and m_d are the isentropic efficiency and mass flow rate of the pump at the design point. $\eta_{p,d}$, m_d and n are given as 0.84, 2500 kg/h and 0.34 in the present model.

3.3. Expander Model

The scroll expander is used in the prototype. The expansion of working fluid in a scroll expander consists of three processes: suction, expansion and exhaust. Thus, the total output work of the expander is the sum of the suction work, expansion work and exhaust work [43]. For a unit mass of working fluid, the suction work according to the energy balance principle is:

$$w_{in} = h_{in} - u_{in} = p_{in}v_{in} \tag{7}$$

where h_{in}, u_{in} and v_{in} are the specific enthalpy, specific internal energy and specific volume of the working fluid at the expander inlet, respectively; and p_{in} is the expander inlet pressure.

The adiabatic and reversible expansion process of the working fluid in the scroll chamber is assumed. In this condition, the expansion work according to the beginning and termination of the expansion is calculated as follows:

$$w_s = u_{in} - u_c = h_{in} - p_{in}v_{in} - (h_c - p_cv_c) \tag{8}$$

where the subscript c in the formula represents the end-of-expansion state of working fluid in the scroll chamber.

The exhaust work is calculated by:

$$w_{ex} = p_dv_c \tag{9}$$

where p_d indicates the exhaust pressure of the expander connected with the pipeline. When the expander operating pressure ratio is not the same as the design pressure ratio, the phenomenon of under-expansion or over-expansion will occur [44]. The deterioration of output work due to the under or over expansion can be considered in Equations (8) and (9).

Considering the internal leakage, mechanical friction and heat loss of the expander, the practical output power of the expander can be expressed as:

$$w_{exp} = \eta_{exp}(w_{in} + w_s - w_{ex}) = \eta_{exp}[h_{in} - h_c + v_c(p_c - p_d)] \tag{10}$$

where η_{exp} is the combined efficiency of the expander and is assumed to be a constant of 0.63.

The actual mass flow rate of the expander is:

$$m_{exp} = \frac{\rho_{in}NV}{60} \tag{11}$$

where N is the speed of the expander and V is the swept volume of the expander.

The thermal efficiency of the ORC system is

$$\eta = \left(w_{exp}m_{exp} - W_p\right)/Q \tag{12}$$

where Q is the power of the evaporator.

3.4. Dynamic Model of the Prototype

By combining the models for every component together, the dynamic model of the cycle is developed as shown in Figure 4. Seven variables need to be solved in the modeling:

the L_1, L_2, pressure, specific enthalpy at the exchanger outlet and wall temperature at each section. In this way, the variation of all operation parameters and performance of the prototype with time could be calculated.

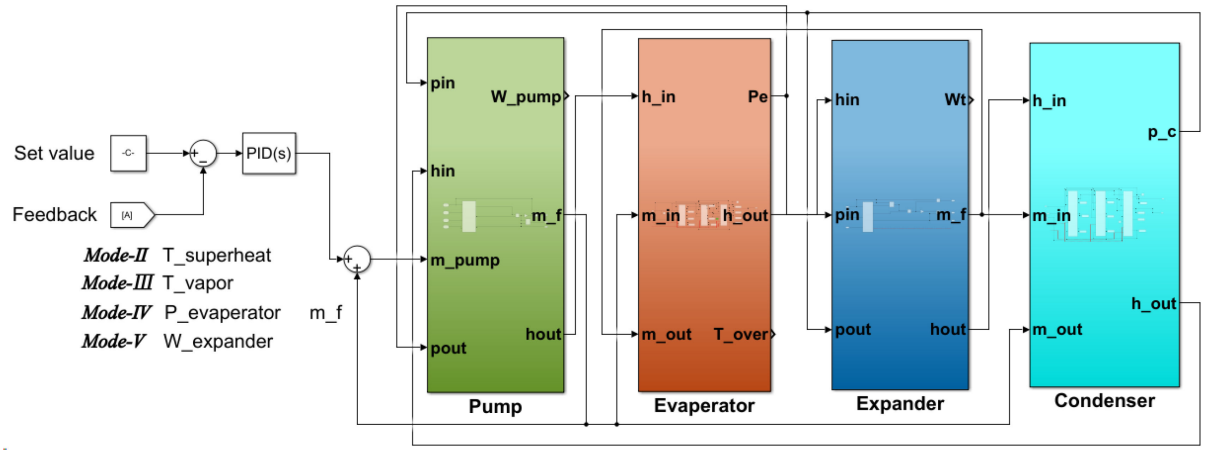

Figure 4. The developed dynamic model of the ORC prototype.

A PID module is adopted to regulate the mass flow rate of the working fluid based on the preset objective in different control strategies. Consequently, the dynamic characteristics of the ORC prototype under different control strategies are simulated and compared.

4. Results and Discussion

4.1. Model Validation

Table 4 gives the main parameters of the ORC prototype at the design point. The performance of the prototype with the heat source temperature varying from 150 to 120 °C was tested and listed in Table 5. The dynamic characteristics of the prototype with the heat source temperature varying from 150 to 140 °C are selected to validate the developed dynamic model. It is seen that the decrease in heat source temperature leads to the gradual deterioration of the ORC performance. The decrease in the condensation pressure is gentle, indicating that the variation of heat source temperature has a limited effect on the condensation process. The isentropic efficiency of the expander is relatively stable, which means the expander can operate stably and effectively under different heat source temperatures.

Table 4. The main parameters of the ORC system at the design point.

Parameters	Value	Parameters	Value
Heat source temperature	150 °C	Working fluid flow rate	800 kg/h
Heat source flow rate	6900 kg/h	Expander rotating speed	1600 rev/min
Cooling water temperature	23 °C	Ambient temperature	23 °C
Cooling water flow rate	3600 kg/h		

Table 5. Off-design performance of the ORC prototype with decreasing heat source temperature.

Heat Source Temperature (°C)	Evaporation Pressure (kPa)	Condensation Pressure (kPa)	Power Load (W)	Vapor Superheat (°C)	Thermal Efficiency (%)	Expander Isentropic Efficiency (%)
149.9	1502.8	308.4	4175	39.2	5.56	54.7
140.6	1452.8	309.2	3969	32.6	5.34	53.9
130.6	1402.8	306.5	3761	25.0	5.21	53.7
120.5	1334.5	301.2	3473	17.1	4.95	52.6

In Figure 5a, it is seen that the predicted evaporation pressure is consistent with the measured one with a relative error of about 0.7%. In Figure 5b, the simulated condensation

pressure is slightly lower than the tested results. In addition, a gradual decrease in the simulated condensation pressure can be seen, while the tested curve is relatively stable.

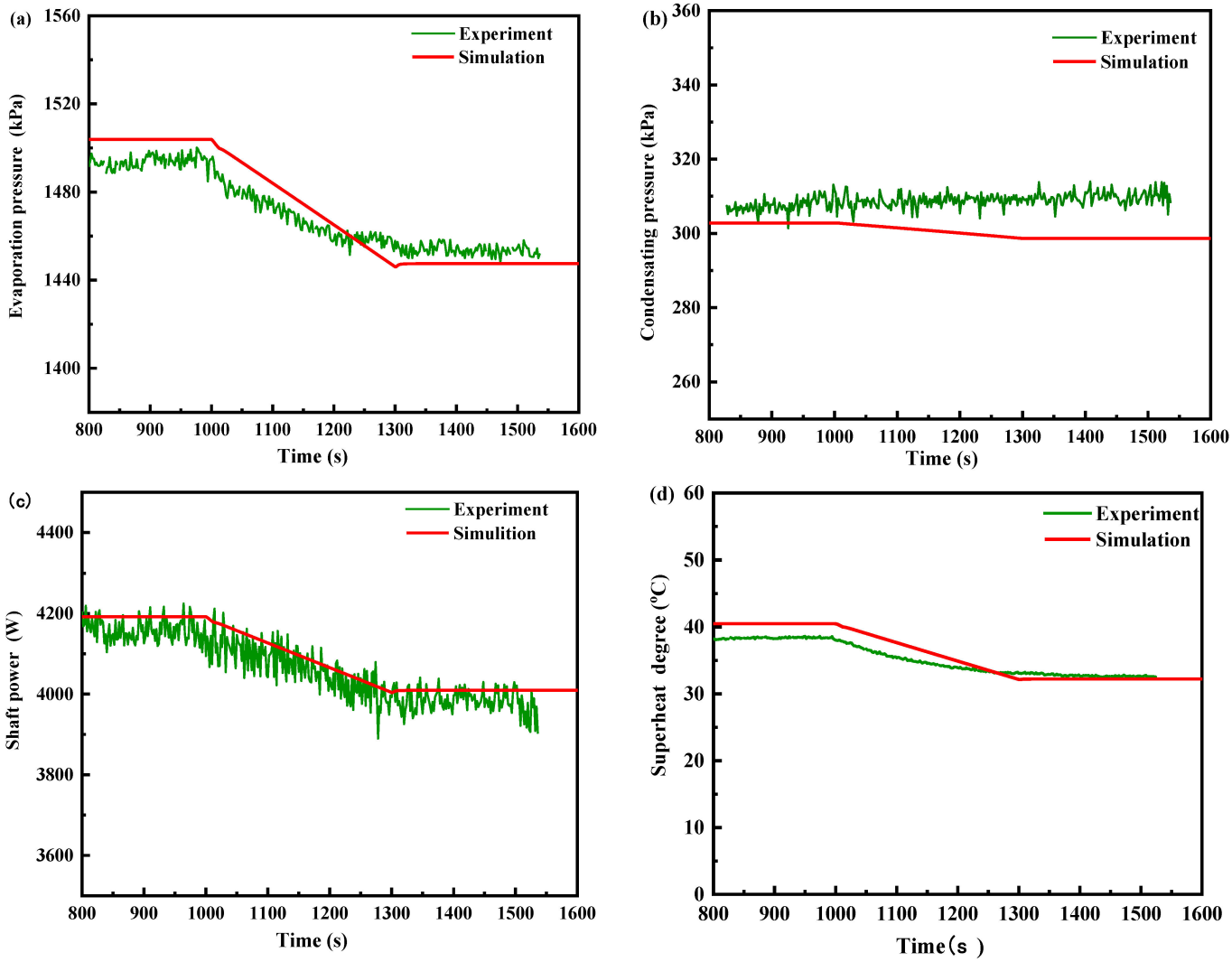

Figure 5. Comparison between the simulation and experimental results of ORC: (**a**) evaporation pressure, (**b**) condensation pressure, (**c**) power and (**d**) superheat degree.

Referring to the condensation pressure in Table 5, we can see that tested condensation pressure has a slight increase of 0.8 kPa. The diverse trend between the tested and simulated condensation pressure is caused by the temperature variation of the cooling water. During the test, the cooling water gradually increases from 23.2 to 23.5 °C, while it is set as a constant of 23 °C in the simulation. It is seen that the condensation pressure is more sensitive to the cooling water temperature than the heat source temperature as the variation of the cooling water temperature can directly change the heat transfer temperature difference.

The relative error between the tested and simulated condensation pressure is 6.2%, which is acceptable for the simulation. The results in Figure 5c exhibit the good agreement between the predicted mechanical shaft power and the tested one with a relative error of about 0.8%. In Figure 5d, the relative error of the vapor superheat degrees between the simulation and the experiment is less than 5%. Generally, Figure 5 shows a good agreement between the simulation results and the experimental data, which ensures the reliable and accurate prediction of the dynamic characteristics of the prototype under various off-design conditions through the present model.

4.2. Comparison of Five Control Strategies for Off-Design Operation

Based on the ORC model established above, this paper adopted the PID control module to adjust the mass flow rate in real-time when the operating conditions of the unit change. Five operation modes were simulated and compared: constant working fluid mass flow rate, the constant vapor superheat, constant vapor temperature, constant evaporation pressure and constant power load.

The abbreviations and preset target parameters for these five control strategies are shown in Table 6. Ambient temperature, heat source temperature and heat source flow rate fluctuations all change the operating conditions of the ORC system. However, the heat source temperature is the most sensitive factor [24,25,31] affecting the operation of the ORC system. Consequently, the focus of this study is the comparison of system performance under various control strategies when the heat source temperature varies.

Table 6. Control strategy abbreviation and preset parameters.

	Control Strategy	Abbreviation	Set
Mode-I	Constant working fluid mass flow rate	**CMFR**	working fluid mass flow rate of 800 kg/h
Mode-II	Constant vapor superheat	**CVS**	superheat degree of 10 °C
Mode-III	Constant vapor temperature	**CVT**	vapor temperature of 130 °C
Mode-IV	Constant evaporation pressure	**CEP**	evaporation pressure of 1.5 MPa
Mode-V	Constant power load	**CPL**	power load of 4 kW

4.2.1. Operation Characteristics under CMFR Mode and CVS Mode

The CVS operation mode is the most commonly used control strategy for the practical ORC unit. For the present tested ORC prototype, the superheat is relatively high at the design point as shown in Table 5. It is seen in Figure 6 that the degree of superheat at the design point is about 40 °C. From the thermodynamic point of view, the relatively smaller superheat degree can benefit the ORC performance. Thus, the operation point of this ORC prototype can be optimized.

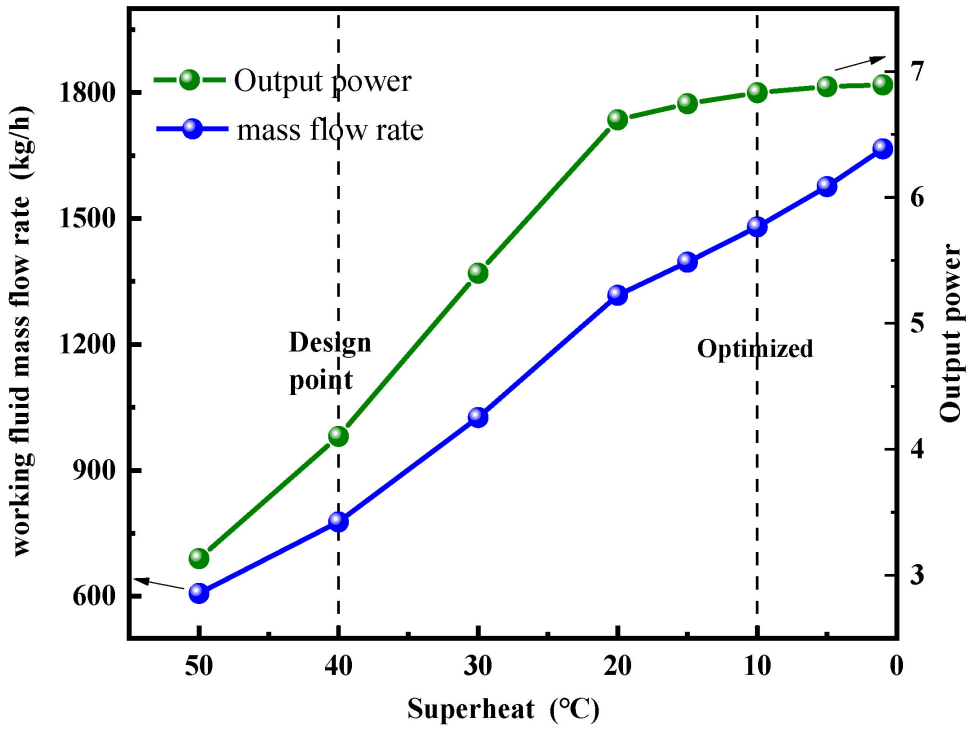

Figure 6. Effect of vapor superheat degrees on the output power of the ORC prototype.

With the increase in the working fluid mass flow rate, the degree of superheat becomes smaller significantly. At the same time, the output power of the ORC unit increases sharply with the superheat degree decreasing from 40 to 20 °C. Then, with the further decrease in superheat degree from 20 to 0 °C, the output power exhibits gentle growth. According to the results in Figure 6, the superheat degree of 10 °C is set as a constraint to ensure both the security operation and relatively high performance of the expander, which refers to the optimized point in the chart.

Figure 7 shows the dynamic response of the key operating parameters of the ORC prototype at CVS mode with a stepwise drop in the heat source temperature. Corresponding to the operating parameters at the optimized point, when the heat source temperature steps down from 150 to 140 °C or from 140 to 130 °C, it is seen that the superheat degrees of the vapor exhibit a sharp decrease within 10 s. The quick response of the superheat degrees is due to a thermal couple of heat source fluid and ORC working fluid in the evaporator.

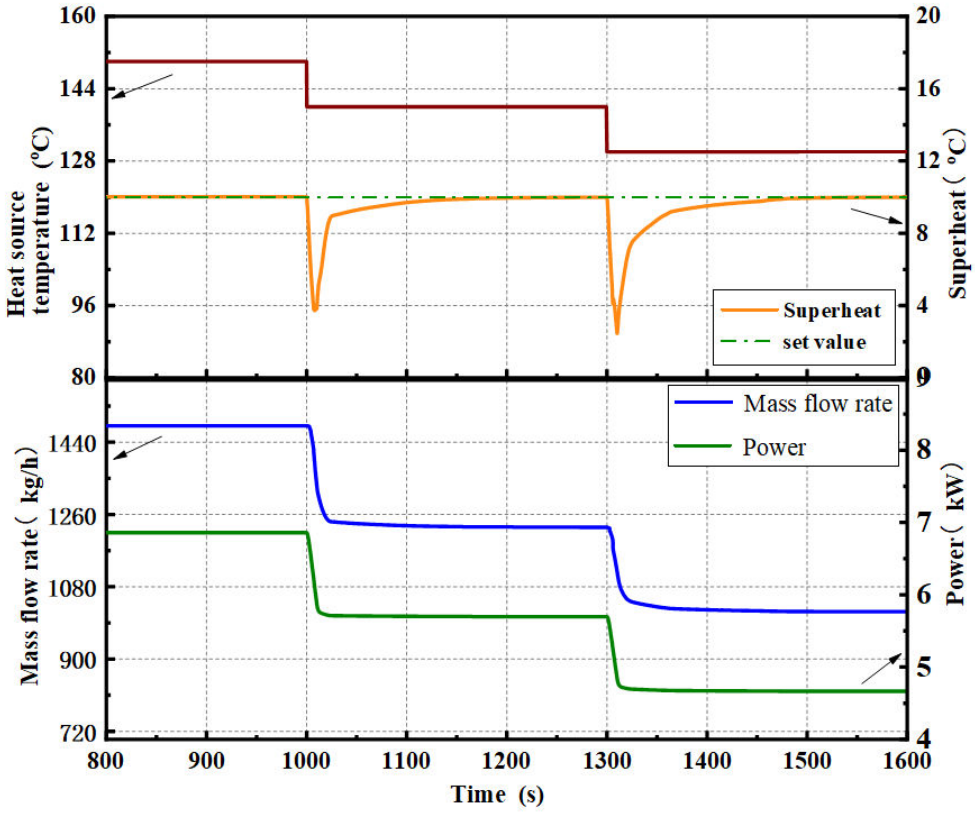

Figure 7. Dynamic response of key operating parameters under the CVS mode.

The counter flow arrangement makes the change of heat source temperature immediately act on the outlet temperature of the working fluid vapor. It is also seen that the mass flow rate of working fluid was reduced by the PID algorism with a 1–2 s delay to the change of the superheat degrees to avoid the liquid droplet entrainment at the expander inlet. The decrease in the mass flow rate leads to a synchronized decline in the output power of the ORC unit and a significant recovery of the superheat degrees. Then, the superheat degrees gradually approach the set value of 10 °C in about 100–150 s.

Figure 8 shows the operating characteristics of the ORC system under CVS mode and CMFR mode. The lower limit of 10 °C superheat degrees is set for the CMFR mode. The working fluid mass flow rate under the CMFR mode is kept the same as that at the design point: 800 kg/h. The dash-dot line in Figure 8a represents the maximum working fluid mass flow rate corresponding to the 0 °C superheat degree. It is clear that the CVS mode can enable the ORC system to work in a large heat source temperature range (150 to 90 °C), while the CMFR mode can only provide relatively narrow range from 150 to 115 °C.

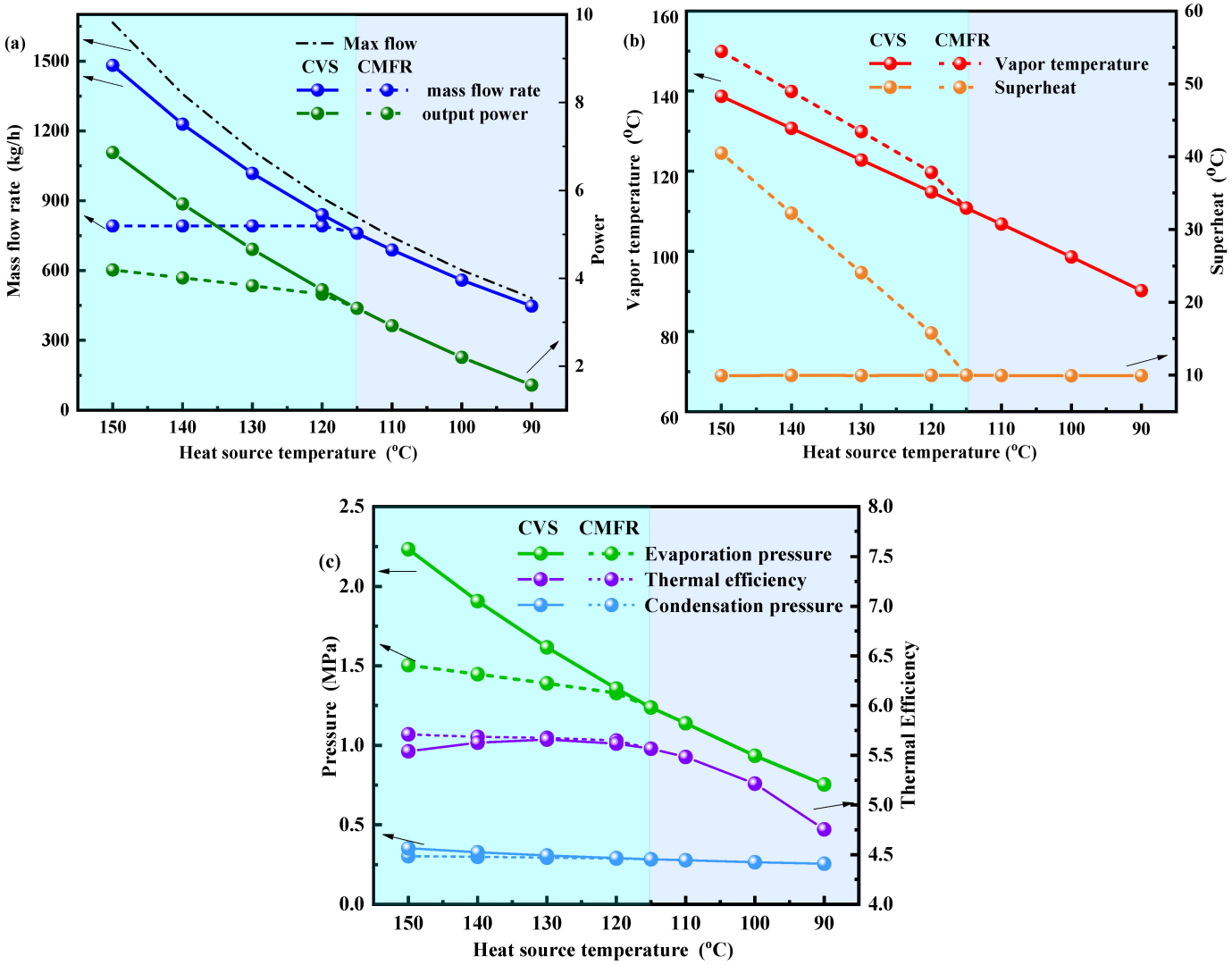

Figure 8. Variation of key parameters of the ORC system with heat source temperature under CVS and CMFR modes. (**a**) mass flow rate and power, (**b**) vapor temperature and superheat, (**c**) vapor pressure and thermal efficiency.

This is because the adjustment of the working fluid mass flow rate at the CVS mode effectively changes the evaporation pressure, shown in Figure 8c, to keep the 10 °C superheat degrees at the expander inlet, seen in Figure 8b. In this condition, the output power is sensitive to the variation of the heat source temperature. It is seen that the output power is reduced from 7 to 1 kW (almost the whole range from none to the maximum) with the heat source temperature decreasing from 150 to 90 °C. Conversely, the CMFR mode offers relatively stable output power and evaporation pressure at the expense of the significantly changed vapor temperature and superheat degrees.

At the heat source temperature of 115 °C, the working fluid mass flow rate at the CVS mode reaches 800 kg/h, which is kept under the CMFR mode. The corresponding superheat degree is 10 °C. This means the CMFR mode cannot apply to the heat source with a temperature lower than 115 °C due to the constraint of at least 10 °C superheat degrees. It is also seen in Figure 8c that the thermal efficiency of both modes for the temperature range from 120 to 140 °C is relatively high and stable.

4.2.2. Operation Characteristics under CVT Mode

As mentioned in Section 4.2.1, the counter flow arrangement of fluids in the evaporator makes the change of heat source temperature immediately reflected on the vapor temperature. If the expander has a limit on the inlet vapor temperature, the CVT mode should be enabled. In this modeling, the inlet vapor temperature of 130 °C is set as the control objective. Consequently, the ORC prototype should work under a heat source temperature higher than 130 °C.

Figure 9 shows the response of key operation parameters under the step jump of heat source temperature from 130 to 140 °C and from 140 to 150 °C. It is seen that vapor temperature at the expander inlet has a short time overshooting just after the 10 °C jump of the heat source temperature. Simultaneously, the superheat degrees also exhibit a slight increase, which triggers the PID algorism to increase the working fluid mass flow rate.

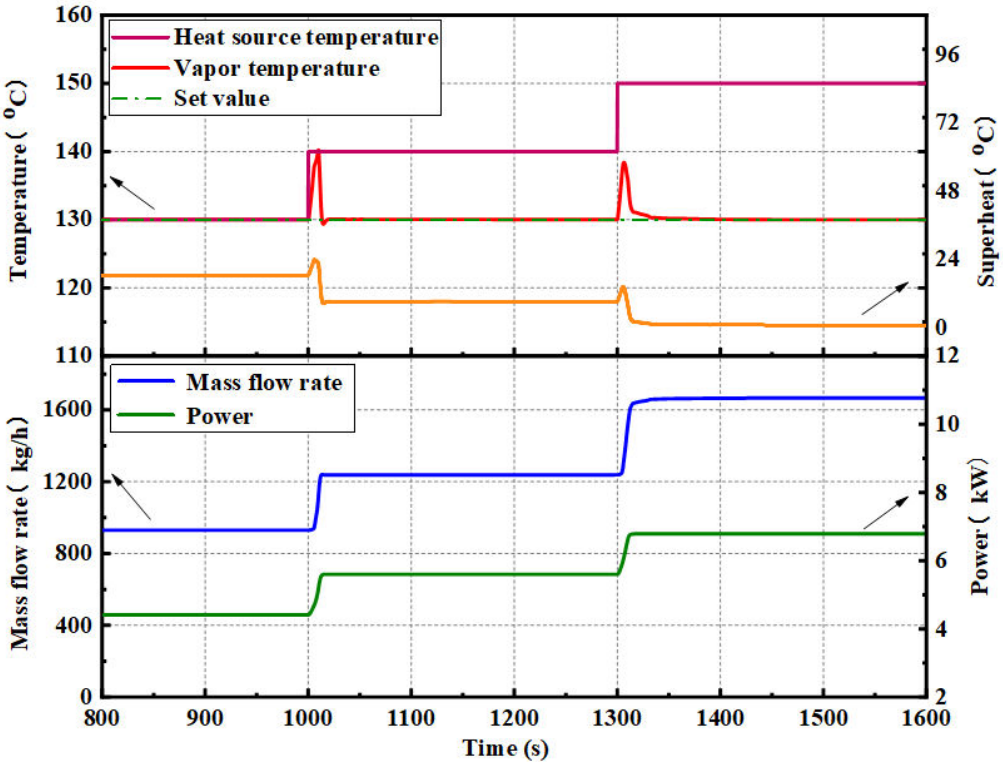

Figure 9. Dynamic response of key operating parameters under the CVT mode.

Then, the output power of the ORC prototype increases, and the superheat degrees decrease. As the heat source temperature is adjusted to 140 °C, the superheat degrees become lower than 10 °C. When the heat source temperature is further increased to 150 °C, the superheat degrees approach zero. This means that the CVT mode can only be applied to a narrow range of the heat source temperature. The upper limit is 150 °C for this mode at the present ORC prototype.

According to the results in Figure 9, the available heat source temperature is from 130 to 150 °C for the CVT mode, which is shown in Figure 10 as the 'CVT region'. If the heat source temperature is higher than 150 °C, the vapor superheat degrees cannot be guaranteed. If the heat source temperature is lower than 130 °C, the vapor temperature of 130 °C cannot be maintained. It has to decline with the heat source temperature. Thus, the CVT mode is transferred to the varied vapor temperature mode, shown as the 'VVT' region in Figure 10.

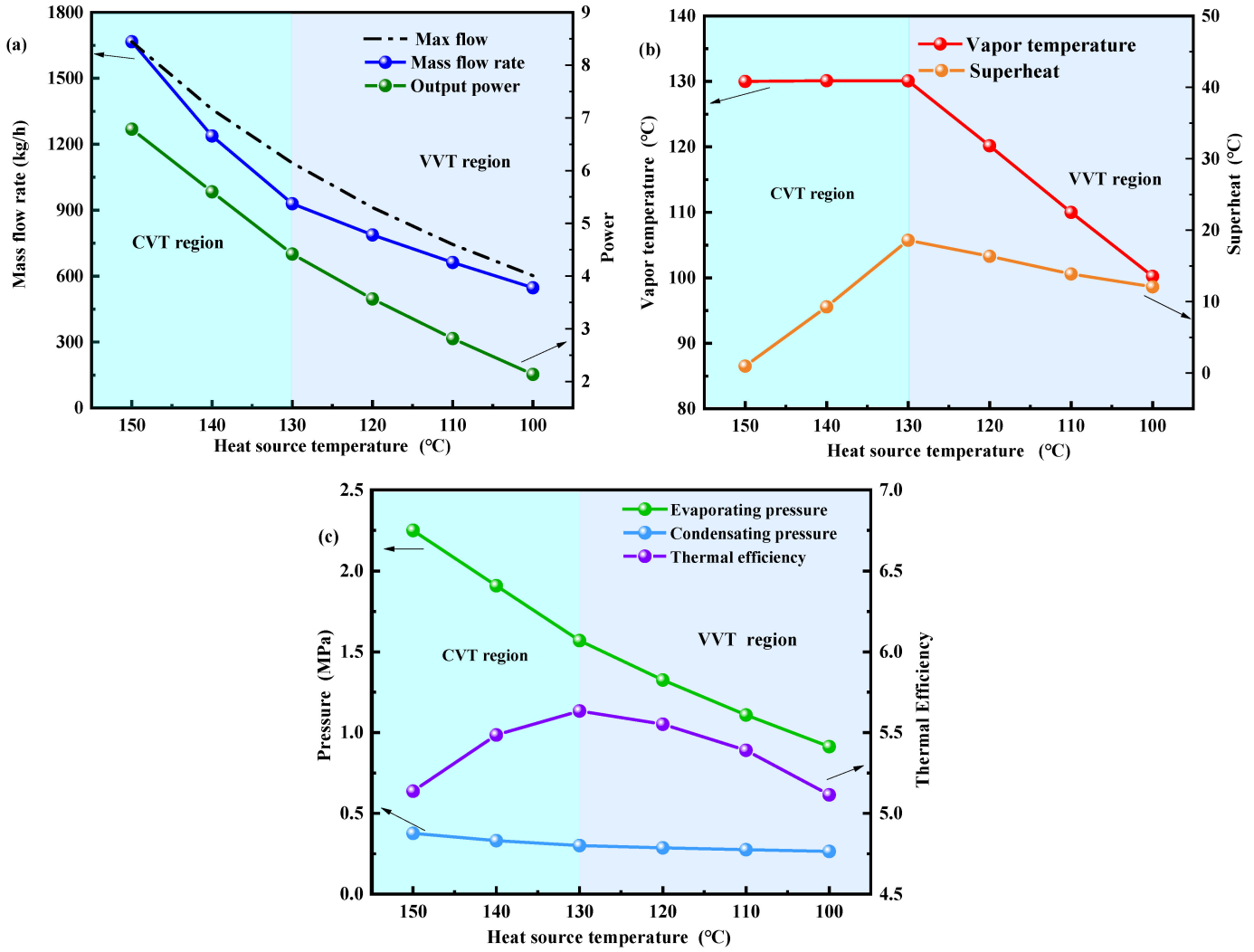

Figure 10. Variation of key parameters of the ORC system with the heat source temperature under CVT mode. (**a**) mass flow rate and power, (**b**) vapor temperature and superheat, (**c**) vapor pressure and thermal efficiency.

With the further decrease in the heat source temperature, the working fluid mass flow rate is reduced and the highest vapor temperature is limited to the heat source temperature. As a result, the output power in Figure 10a, the superheat degree in Figure 10b, and the evaporation pressure and thermal efficiency in Figure 10c gradually decrease with the decrease in heat source temperature. Considering the CVT and the VVT regions together, it is seen that the output power of the expander decreases almost linearly with the decreasing heat source temperature.

However, the thermal efficiency reaches the highest efficiency of 5.7% with the heat source temperature decreasing from 150 to 130 °C. This is caused by the reduction of the power consumed by the pump with the decrease in the working fluid mass flow rate. Comparing the results in Figure 10 to those in Figure 8, we can see that the output power under CVT mode is slightly lower than that under the CVS mode at a specific heat source temperature. This indicates that the high vapor superheat under the CVT is harmful to the cycle performance.

4.2.3. Operation Characteristics under CEP Mode

The CEP mode of the ORC prototype is similar to the fixed pressure operation of the traditional steam unit. In the present work, the evaporation pressure was fixed at 1.5 MPa.

The dynamic response of key operation parameters under this mode with the stepwise drop of the heat source temperature from 150 to 140 °C and from 140 to 130 °C is shown in Figure 11. Once the heat source temperature decreases by the step of 10 °C, the reduced temperature difference between the heat source fluid and the ORC working fluid results in the reduction of heat flux of the evaporator.

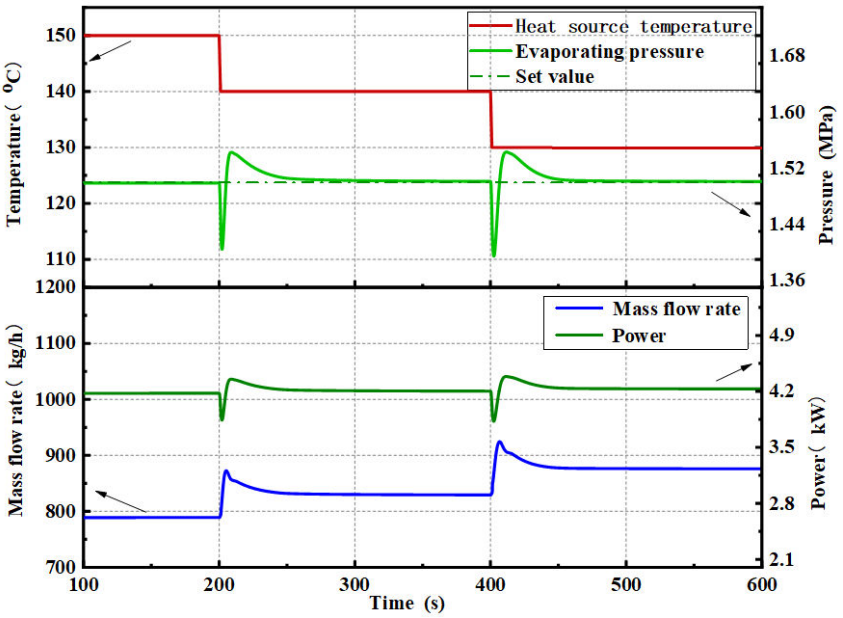

Figure 11. Dynamic response of key operating parameters under the CEP mode.

Consequently, the amount of vapor gathering in the evaporator becomes smaller, which is reflected by the sharp decrease in the evaporation pressure. The PID algorithm presently responds to the change of evaporation pressure and increases the working fluid mass flow rate through the pump. Then, the evaporation pressure climbs back in a few seconds and exhibits a slight overshooting. It takes about 50 s for the evaporation pressure to approach the next steady state. The evaporation pressure is directly related to the driving force of the expander. Thus, the output power of the ORC prototype showed a similar trend to the evaporation pressure.

Figure 12 shows the effect of heat source temperature on the operation characteristics of the ORC prototype under the CEP mode. It is seen that the CEP mode is available only if the heat source temperature is higher than 125 °C. The further reduction of the heat source temperature cannot provide enough amount of vapor in the evaporator to maintain the target pressure and the superheat degree at the evaporator outlet will be too low. Hence, the control strategy is transferred to the CVS mode to keep the 10 °C superheat degrees.

When the ORC prototype operates under the CEP mode, as shown in Figure 12a, the working fluid mass flow rate is gradually raised with the reduction of heat source temperature to maintain the preset evaporation pressure by making the liquid phase occupy more space in the evaporator. In this condition, the output power is stable because the fixed evaporation pressure provides the stable driving force as mentioned above.

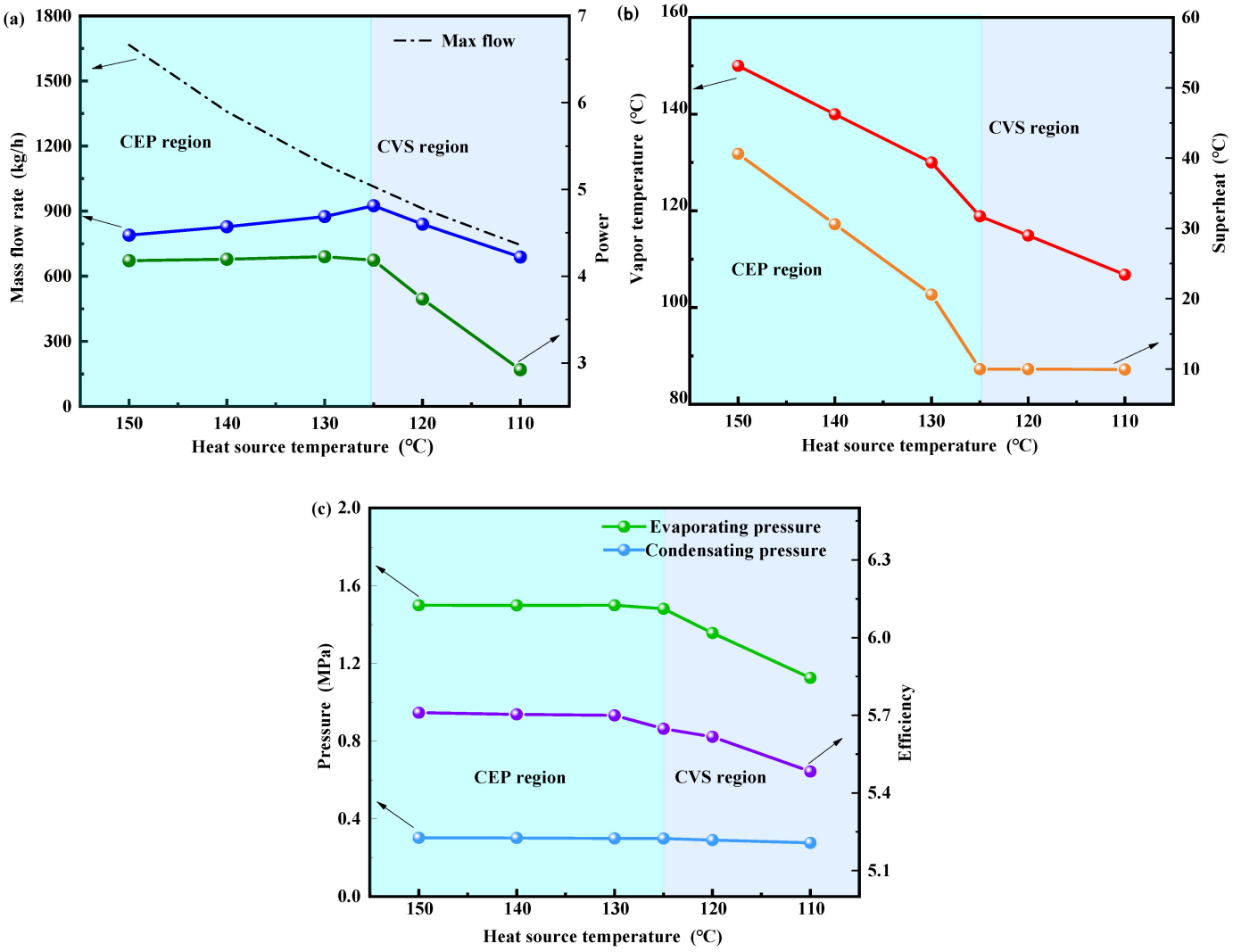

Figure 12. Variation of key parameters of the ORC system with heat source temperature under CVS and CEP modes. (**a**) mass flow rate and power, (**b**) vapor temperature and superheat, (**c**) vapor pressure and thermal efficiency.

However, the weakened heat transfer capacity of the evaporator at lower heat source temperature leads to a significant decrease in the vapor temperature and the superheat degrees as shown in Figure 12b. The thermal efficiency in Figure 12c is also stable under the CEP mode. These results reflect that the CEP mode can offer relatively stable ORC performance as long as it is available for the heat source condition.

4.2.4. Operation Characteristics under CPL Mode

Some application scenarios require the ORC unit to provide relatively stable output power. In the present simulation, the output power of the ORC prototype is preset as 4 kW for the CPL mode. The dynamic response of key operation parameters under this mode with the stepwise drop of the heat source temperature from 150 to 140 °C and from 140 to 130 °C is shown in Figure 13. It is seen that the dynamic response and adjustment of the prototype are similar to that of the CEP mode but are more dramatic and faster.

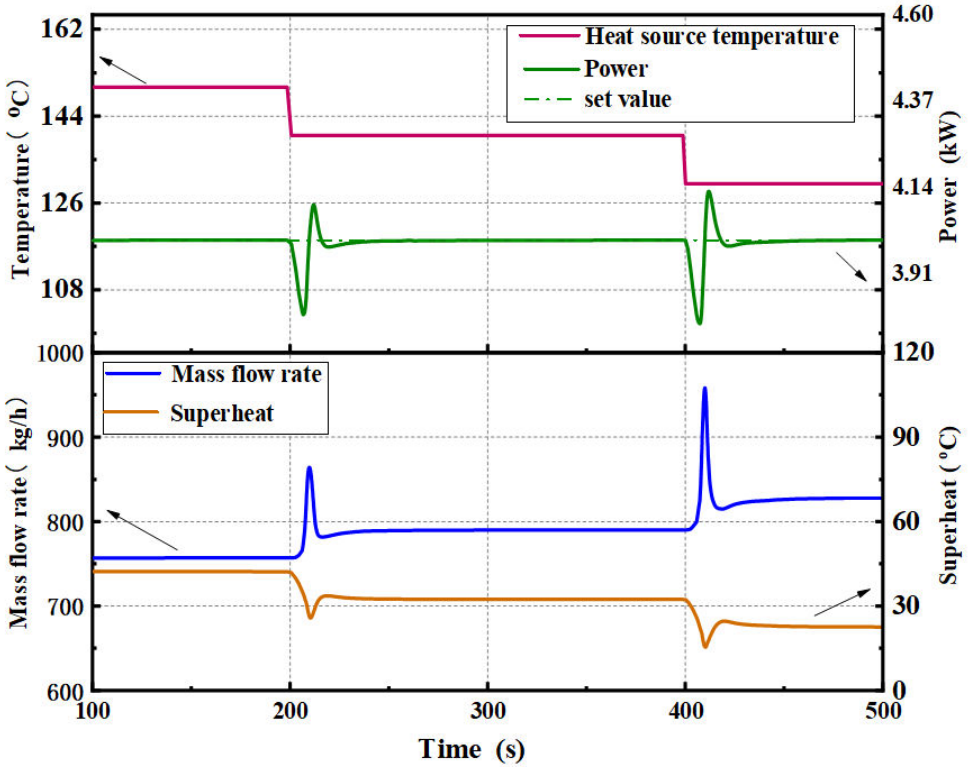

Figure 13. Dynamic response of key operating parameters under the CPL mode.

As the heat source temperature steps down, the reduced heat transfer capacity of the evaporator cannot provide sufficient amounts of vapor to drive the expander, reflected by the sharp decrease in the output power. The PID algorithm presently detects the reduction of output power and responds to a sharp increase in the working fluid mass flow rate.

The overcontrol occurs to quickly recover the output power and then results in the overshooting. It takes about 30 s for the output power to approach the next steady-state. The restabilized mass flow rate becomes higher and the superheat degrees are decreased. It is also seen that the dynamic behavior of the ORC prototype is more sensitive to the change of heat source temperature when the heat source temperature is lower.

Figure 14 shows the influence of heat source temperature on the performance of the ORC prototype under CPL mode. It is seen that the results in Figure 14 have similar trends to Figure 12. The operation of the ORC prototype is divided into two modes by the heat source temperature of 125 °C. The CPL mode is available when the heat source temperature is higher than 125 °C, while it should turn into the CVS mode for the further reduction of the heat source temperature due to the significant decrease in the superheat degree at the evaporator outlet as shown in Figure 14b.

When the ORC prototype operates under the CPL mode, as shown in Figure 14a, the working fluid mass flow rate is gradually increased with the decrease in the heat source temperature to keep the power load stable. It is seen that the evaporation pressure is also stable. The reason for this phenomenon is discussed in the above section. In addition, the decrease in the heat source temperature leads to a significant decrease in the vapor temperature and the superheat degrees as shown in Figure 14b.

The further reduction of the heat transfer capacity of the evaporator at a heat source temperature lower than 125 °C cannot vaporize a sufficient amount of vapor corresponding to the given working fluid mass flow rate. Consequently, the evaporation pressure and the output power cannot be maintained. In this condition, the control strategy of CVS mode is preferred to maintain the 10 °C superheat degrees by reducing the mass flow rate and evaporation pressure as seen in Figure 14a,c. The thermal efficiency in Figure 14c is also stable under the CPL mode. The results of the CEP and CPL mode are similar and imply

that both these two modes can provide relatively stable ORC performance when the heat source temperature is proper.

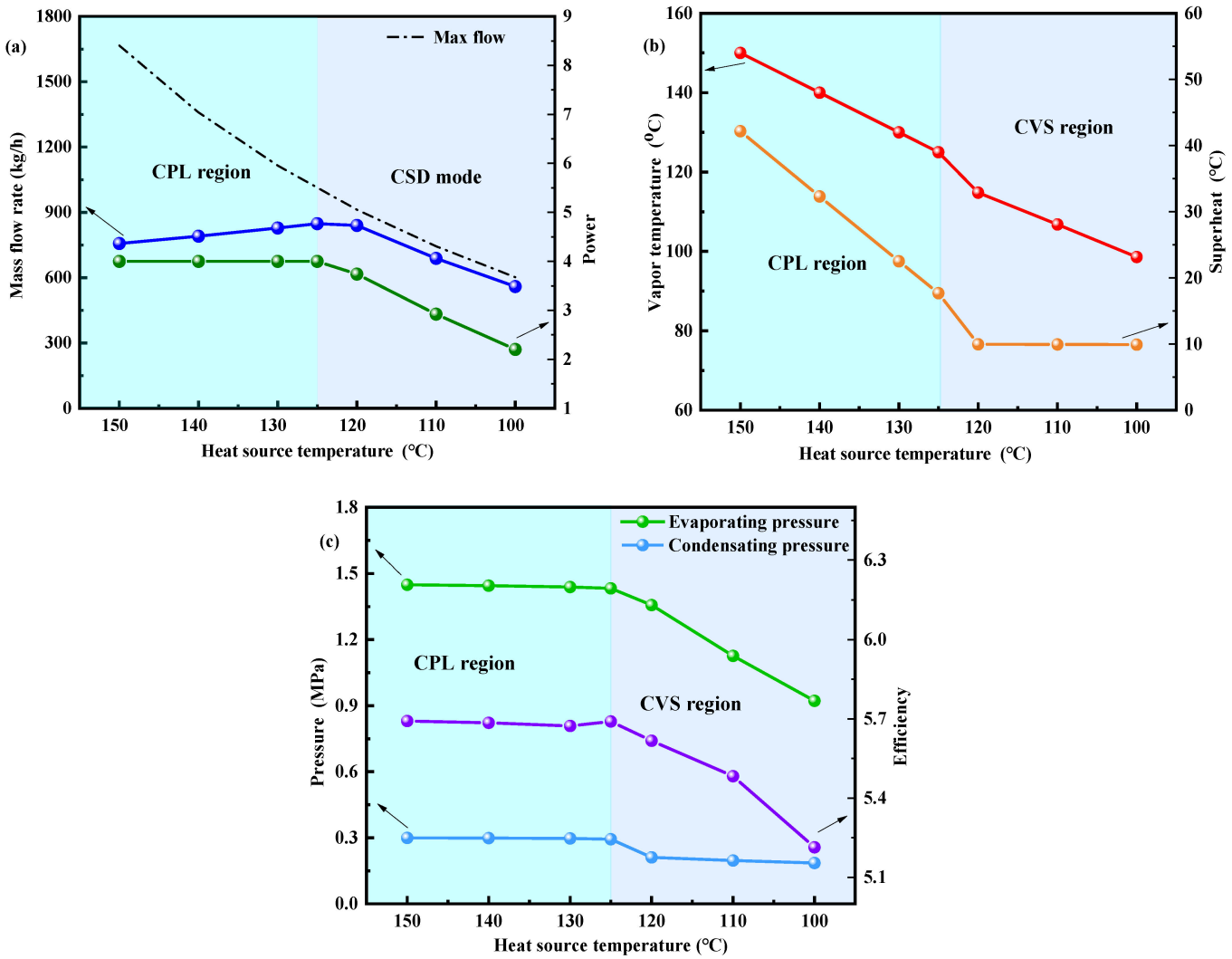

Figure 14. Variation of key parameters of the ORC system with heat source temperature under CVS and CPL modes. (**a**) mass flow rate and power, (**b**) vapor temperature and superheat, (**c**) vapor pressure and thermal efficiency.

5. Conclusions

To investigate the effect of different control strategies on the dynamic response and operation characteristics of an ORC system driven by a heat source with variable temperatures, the present work developed a transient model and compared five typical control strategies. The model was validated by experimental data of a 4 kW ORC prototype. The simulation was performed under the constraint that the working fluid at the expander inlet should be superheated. The main contributions of this paper are summarized as follows:

1. The adjustment of the working fluid mass flow rate through the PID algorism can satisfy the dynamic operation of the ORC unit. The system approached the next steady-state within 50 s for most operation modes.
2. The CVS mode enabled the safe operation of the ORC system under the largest range of heat source temperature, while the other four modes were only available for a certain temperature range—higher than 125 or 130 °C. The further decrease in the heat source temperature compelled the system to turn to other control strategies—generally, the CVS mode—to guarantee the safe operation of the ORC system.

3. In addition to the CPL mode, the CEP mode can also provide relatively stable output power of the ORC system at various heat source temperatures, while the CVT and CVS modes exhibited significant variation of the output power. The CMFR mode is the simplest control strategy and showed a moderate change of the output power with heat source temperature.
4. The variation of the thermal efficiency is limited when the heat source temperature is higher than 125 °C, except for with the CVT mode. Considering the high performance and stable operation of the ORC system, it is necessary to have different operation modes combined in the control strategy according to the specific working scenarios.

Author Contributions: Conceptualization, Y.Z. and Z.M.; writing, original draft preparation, Y.Z. and G.H.; writing, review and editing, J.R.; supervision, G.H. and Z.M. All authors have read and agreed to the published version of the manuscript.

Funding: This research was funded by the National Key R&D Program of China (2019YFC1907002) and the National Natural Science Foundation of China (No. 51776064).

Acknowledgments: The authors highly appreciate the support of the National Key R&D Program of China (2019YFC1907002) and the National Natural Science Foundation of China (No. 51776064).

Conflicts of Interest: The authors declare no conflict of interest including any financial, personal or other relationships with other people or organizations.

Nomenclature

a	chevron angle, (rad)	w	specific power, (kJ/kg)
Bo	the boiling number	Greek letters	
b	corrugation pitch,(m)	α	heat transfer coefficient
c	specific heat, (J/kg·K)	η	efficiency
d	thickness, (m)	ρ	density, (kg/m^3)
de	hydraulic diameter, (m)		
h	specific enthalpy, (J/kg·K)	Subscripts	
L	length, (m)	c	the end-of-expansion state
m	mass flow rate, (kg/h)	d	design
N	notating speed, (rev/min)	e	evaporation
Nu	the Nusselt number	ex	exhaust
P	pressure, (kPa)	exp	expander
Pr	the Prandtl number	f	fluid
Pd	back pressure, (kPa)	g	gas
Q	heat power, (kW)	i	inside
Re	the Reynolds number	in	inlet
s	specific entropy, (J/kg·K)	l	Liquid phase
T	temperature, (°C)	o	outside
t	time, (s)	p	pump
u	specific internal energy, (J/kg·K)	tp	two-phase
V	volume, (m^3)	s	isentropic process
v	specific volume, (m^3/kg)	v	vapor phase
W	power, (kW)	w	wall

References

1. Braimakis, K.; Karellas, S. Exergetic optimization of double stage Organic Rankine Cycle (ORC). *Energy* **2018**, *149*, 296–313. [CrossRef]
2. Tchanche, B.F.; Papadakis, G.; Lambrinos, G.; Frangoudakis, A. Fluid selection for a low-temperature solar organic Rankine cycle. *Appl. Therm. Eng.* **2009**, *29*, 2468–2476. [CrossRef]
3. Hu, S.Z.; Li, J.; Yang, F.B.; Yang, Z.; Duan, Y.Y. Multi-objective optimization of organic Rankine cycle using hydrofluorolefins (HFOs) based on different target preferences. *Energy* **2020**, *203*, 117848. [CrossRef]
4. Swierzewski, M.; Kalina, J. Optimisation of biomass-fired cogeneration plants using ORC technology. *Renew. Energy* **2020**, *159*, 195–214. [CrossRef]
5. Vera, D.; Baccioli, A.; Jurado, F.; Desideri, U. Modeling and optimization of an ocean thermal energy conversion system for remote islands electrification. *Renew. Energy* **2020**, *162*, 1399–1414. [CrossRef]

6. Frate, G.F.; Baccioli, A.; Lucchesi, E.; Ferrari, L. ORC Optimal Design through Clusterization for Waste Heat Recovery in Anaerobic Digestion Plants. *Appl. Sci.* **2021**, *11*, 2762. [CrossRef]
7. Shu, G.Q.; Liu, L.N.; Tian, H.; Wei, H.Q.; Yu, G.P. Parametric and working fluid analysis of a dual-loop organic Rankine cycle (DORC) used in engine waste heat recovery. *Appl. Energy* **2014**, *113*, 1188–1198. [CrossRef]
8. Liu, P.; Shu, G.Q.; Tian, H. How to approach optimal practical Organic Rankine cycle (OP-ORC) by configuration modification for diesel engine waste heat recovery. *Energy* **2019**, *174*, 543–552. [CrossRef]
9. Chen, G.B.; An, Q.S.; Wang, Y.Z.; Zhao, J.; Chang, N.N.; Alvi, J. Performance prediction and working fluids selection for organic Rankine cycle under reduced temperature. *Appl. Therm. Eng.* **2019**, *153*, 95–103. [CrossRef]
10. Yang, F.B.; Cho, H.J.; Zhang, H.G.; Zhang, J. Thermoeconomic multi-objective optimization of a dual loop organic Rankine cycle (ORC) for CNG engine waste heat recovery. *Appl. Energy* **2017**, *205*, 1100–1118. [CrossRef]
11. Guzovic, Z.; Raskovic, P.; Blataric, Z. The comparision of a basic and a dual-pressure ORC (Organic Rankine Cycle): Geothermal Power Plant Velika Ciglena case study. *Energy* **2014**, *76*, 175–186. [CrossRef]
12. Emadi, M.A.; Chitgar, N.; Oyewunmi, O.A.; Markides, C.N. Working-fluid selection and thermoeconomic optimisation of a combined cycle cogeneration dual-loop organic Rankine cycle (ORC) system for solid oxide fuel cell (SOFC) waste-heat recovery. *Appl. Energy* **2020**, *261*, 114384. [CrossRef]
13. Bekiloglu, H.E.; Bedir, H.; Anlas, G. Multi-objective optimization of ORC parameters and selection of working fluid using preliminary radial inflow turbine design. *Energy Convers. Manag.* **2019**, *183*, 833–847. [CrossRef]
14. Ceglia, F.; Marrasso, E.; Roselli, C.; Sasso, M. Effect of layout and working fluid on heat transfer of polymeric shell and tube heat exchangers for small size geothermal ORC via 1-D numerical analysis. *Geothermics* **2021**, *95*, 102118. [CrossRef]
15. Li, P.; Mei, Z.K.; Han, Z.H.; Jia, X.Q.; Zhu, L.; Wang, S. Multi-objective optimization and improved analysis of an organic Rankine cycle coupled with the dynamic turbine efficiency model. *Appl. Therm. Eng.* **2019**, *150*, 912–922. [CrossRef]
16. Fu, B.R.; Hsu, S.W.; Lee, Y.R.; Hsieh, J.C.; Chang, C.M.; Liu, C.H. Effect of off-design heat source temperature on heat transfer characteristics and system performance of a 250-kW organic Rankine cycle system. *Appl. Therm. Eng.* **2014**, *70*, 7–12. [CrossRef]
17. Feng, Y.Q.; Hung, T.C.; Wu, S.L.; Lin, C.H.; Li, B.X.; Huang, K.C.; Qin, J. Operation characteristic of a R123-based organic Rankine cycle depending on working fluid mass flow rates and heat source temperatures. *Energy Convers. Manag.* **2017**, *131*, 55–68. [CrossRef]
18. Du, Y.; Yang, Y.; Hu, D.S.; Hao, M.T.; Wang, J.F.; Dai, Y.P. Off-design performance comparative analysis between basic and parallel dual-pressure organic Rankine cycles using radial inflow turbines. *Appl. Therm. Eng.* **2018**, *138*, 18–34. [CrossRef]
19. Manente, G.; Toffolo, A.; Lazzaretto, A.; Paci, M. An Organic Rankine Cycle off-design model for the search of the optimal control strategy. *Energy* **2013**, *58*, 97–106. [CrossRef]
20. Hu, D.; Zheng, Y.; Wu, Y.; Li, S.; Dai, Y. Off-design performance comparison of an organic Rankine cycle under different control strategies. *Appl. Energy* **2015**, *156*, 268–279. [CrossRef]
21. Van Putten, H.; Colonna, P. Dynamic modeling of steam power cycles: Part II—Simulation of a small simple Rankine cycle system. *Appl. Therm. Eng.* **2007**, *27*, 2566–2582. [CrossRef]
22. Wei, D.; Lu, X.; Lu, Z.; Gu, J. Dynamic modeling and simulation of an Organic Rankine Cycle (ORC) system for waste heat recovery. *Appl. Therm. Eng.* **2008**, *28*, 1216–1224. [CrossRef]
23. Quoilin, S.; Aumann, R.; Grill, A.; Schuster, A.; Lemort, V.; Spliethoff, H. Dynamic modeling and optimal control strategy of waste heat recovery Organic Rankine Cycles. *Appl. Energy* **2011**, *88*, 2183–2190. [CrossRef]
24. Wang, X.; Shu, G.Q.; Tian, H.; Liu, P.; Li, X.Y.; Jing, D.Z. Engine working condition effects on the dynamic response of organic Rankine cycle as exhaust waste heat recovery system. *Appl. Therm. Eng.* **2017**, *123*, 670–681. [CrossRef]
25. Usman, M.; Imran, M.; Lee, D.H.; Park, B.S. Experimental investigation of off-grid organic Rankine cycle control system adapting sliding pressure strategy under proportional integral with feed-forward and compensator. *Appl. Therm. Eng.* **2017**, *110*, 1153–1163. [CrossRef]
26. Jolevski, D.; Bego, O.; Sarajcev, P. Control structure design and dynamics modelling of the organic Rankine cycle system. *Energy* **2017**, *121*, 193–204. [CrossRef]
27. Wu, X.L.; Chen, J.H.; Xie, L. Integrated operation design and control of Organic Rankine Cycle systems with disturbances. *Energy* **2018**, *163*, 115–129. [CrossRef]
28. Badescu, V.; Aboaltabooq, M.H.K.; Pop, H.; Apostol, V.; Prisecaru, M.; Prisecaru, T. Avoiding malfunction of ORC-based systems for heat recovery from internal combustion engines under multiple operation conditions. *Appl. Therm. Eng.* **2019**, *150*, 977–986. [CrossRef]
29. Chen, X.X.; Liu, C.; Li, Q.B.; Wang, X.R.; Xu, X.X. Dynamic analysis and control strategies of Organic Rankine Cycle system for waste heat recovery using zeotropic mixture as working fluid. *Energy Convers. Manag.* **2019**, *192*, 321–334. [CrossRef]
30. Pei, G.; Li, J.; Li, Y.Z.; Wang, D.Y.; Ji, J. Construction and dynamic test of a small-scale organic rankine cycle. *Energy* **2011**, *36*, 3215–3223. [CrossRef]
31. Li, M.Q.; Wang, J.F.; He, W.F.; Gao, L.; Wang, B.; Ma, S.L.; Dai, Y.P. Construction and preliminary test of a low-temperature regenerative Organic Rankine Cycle (ORC) using R123. *Renew. Energy* **2013**, *57*, 216–222. [CrossRef]
32. Li, J.; Pei, G.; Li, Y.Z.; Wang, D.Y.; Ji, J. Energetic and exergetic investigation of an organic Rankine cycle at different heat source temperatures. *Energy* **2012**, *38*, 85–95. [CrossRef]

33. Zhang, Y.-F.; Li, M.-J.; Ren, X.; Duan, X.-Y.; Wu, C.-J.; Xi, H.; Feng, Y.-Q.; Gong, L.; Hung, T.-C. Effect of heat source supplies on system behaviors of ORCs with different capacities: An experimental comparison between the 3 kW and 10 kW unit. *Energy* **2022**, *254*, 124267. [CrossRef]
34. Miao, Z.; Yang, X.F.; Xu, J.L.; Zou, J.H. Development and dynamic characteristics of an Organic Rankine Cycle. *Chin. Sci. Bull.* **2014**, *59*, 4367–4378. [CrossRef]
35. Wei, D.H.; Lu, X.S.; Lu, Z.; Gu, J.M. Performance analysis and optimization of organic Rankine cycle (ORC) for waste heat recovery. *Energy Convers. Manag.* **2007**, *48*, 1113–1119. [CrossRef]
36. Imran, M.; Pili, R.; Usman, M.; Haglind, F. Dynamic modeling and control strategies of organic Rankine cycle systems: Methods and challenges. *Appl. Energy* **2020**, *276*, 115537. [CrossRef]
37. Das, S.K.; Spang, B.; Roetzel, W. Dynamic Behavior of Plate Heat Exchangers—Experiments and Modeling. *J. Heat Transf.* **1995**, *117*, 859–864. [CrossRef]
38. Kuo, W.S.; Lie, Y.M.; Hsieh, Y.Y.; Lin, T.F. Condensation heat transfer and pressure drop of refrigerant R-410A flow in a vertical plate heat exchanger. *Int. J. Heat Mass Transf.* **2005**, *48*, 5205–5220. [CrossRef]
39. Yan, Y.-Y.; Lio, H.-C.; Lin, T.-F. Condensation heat transfer and pressure drop of refrigerant R-134a in a plate heat exchanger. *Int. J. Heat Mass Transf.* **1999**, *42*, 993–1006. [CrossRef]
40. Han, D.-H.; Lee, K.-J.; Kim, Y.-H. Experiments on the characteristics of evaporation of R410A in brazed plate heat exchangers with different geometric configurations. *Appl. Therm. Eng.* **2003**, *23*, 1209–1225. [CrossRef]
41. Wang, J.; Wang, M.; Li, M.; Xia, J.; Dai, Y. Multi-objective optimization design of condenser in an organic Rankine cycle for low grade waste heat recovery using evolutionary algorithm. *Int. Commun. Heat Mass Transf.* **2013**, *45*, 47–54. [CrossRef]
42. Yan, Y.Y.; Lin, T.F. Evaporation heat transfer and pressure drop of Refrigerant R-134a in a plate heat exchanger. *J. Heat Transf.* **1999**, *121*, 118–127. [CrossRef]
43. Lemort, V.; Quoilin, S.; Cuevas, C.; Lebrun, J. Testing and modeling a scroll expander integrated into an Organic Rankine Cycle. *Appl. Therm. Eng.* **2009**, *29*, 3094–3102. [CrossRef]
44. Quoilin, S.; Lemort, V.; Lebrun, J. Experimental study and modeling of an Organic Rankine Cycle using scroll expander. *Appl. Energy* **2010**, *87*, 1260–1268. [CrossRef]